# Supplementary information for droplet tilings in precessive fields: hysteresis, elastic defects, and annealing

June 10, 2024

Anton Molina[a,b,†], Manu Prakash[b,*]

[a]Department of Materials Science and Engineering, [b]Department of Bioengineering

Stanford University, 450 Serra Mall, Stanford, California 94305

[*] To whom correspondence should be addressed; E-mail: manup@stanford.edu

[†] Present address: b.next, 135 Mississippi Street, San Francisco, California 94107, USA

This supplementary file includes:

- Supplementary Figures 1-10
- Supplementary Videos 1-6

# 1 Control of rotary actuated Stweart Platform

The rotary actuated Stewart platform [1, 2] consists of 6 servo motors (Dynamixel AX-12A, Robotis) controlled by an Arduino compatibile microcontroller (Arbotix-M Robocontroller, Trossen Robotics). The servos labelled $i = 1 - 6$ and are arranged in 3 pairs separated by $120°C$. To coordinate the motion of the 6 servo motors so as to produce a precessing gravity vector, each of the $n$ pairs is given a phase offset of $2n\pi/3$. The motion of the platform can then be controlled with a specified amplitude $A$ and period $T$ to give an angle update $\beta$

$$\beta = A\cos\left(\frac{2\pi t}{T} + \frac{2n\pi}{3}\right) \tag{1}$$

This update is converted into microseconds and sent to the $i^{th}$ motor which is incremented depending on its location:

$$\beta_{t+1}^{(i)} = \begin{cases} \beta_t^i + \beta & i, even \\ \beta_t^i - \beta & i, odd \end{cases} \tag{2}$$

The orientation of the platform is measured in two ways. First a bulls-eye spirit level is used as a check to ensure that the platform is level for static experiments. Second, a BNO-055 digital accelerometer (Bosch Sensortec GmbH, Germany) is used to measure the time evolution of the field during experiments. The sensor is configured to report quaternion values $(w, x, y, z)$ which can be used to construct a three dimension rotation matrix for every time step:

$$Q = \begin{pmatrix} w^2 + x^2 + y^2 + z^2 & 2(xy - wz) & 2(wy + xz) \\ 2(xy + wz) & w^2 - x^2 + y^2 - z^2 & 2(-wx + yz) \\ 2(-wy + xz) & 2(wx + yz) & w^2 - x^2 - y^2 + z^2 \end{pmatrix} \tag{3}$$

The matrix $Q$ can be used to obtain an orientation vector $\mathbf{v}$ by through multiplication of the unit vector normal $\mathbf{n} = [0, 0, 1]^T$ to the platform surface in a flat configuration. The tilt

angle $\alpha$ between this normal vector and the orientation vector is calculated according to:

$$\alpha = \arccos\left(\frac{\mathbf{v}\cdot\mathbf{n}}{\|\mathbf{v}\|\|\mathbf{n}\|}\right) \tag{4}$$

Two dimensional projections of the field are obtained by taking the $x, y$ components of $\mathbf{v}$ and converted to an angle $\theta = \arctan(y/x)$. The input function $u$ is defined as the cosine of $\theta$ relative to the unit vector $\mathbf{n} = [0, 1]^T$ and can take values between -1 and 1.

# 2 Experimental determination of transition angle for isolated vertex

The angle at which an isolated triplet structure would break was determined experimentally. Here, large (4" x 3") glass slides (Ted Pella, USA) were used. The slides were cleaned and treated with air plasma immediately before use. The hydrophobic boundary was made using ink from a multisurface permanent marker (Sharpie™). The pattern was created by programming an automated plotter/cutter (Roland32 Camm1-Servo) with CAD tools. Previous work has shown there to be negligible difference between boundaries formed from permanent ink versus thiol-treated gold [3]. Stable triplet structures were formed by pipetting 2 $\mu L$ of 30% PG solution onto the surface. After the configurations were seeded, glass substrate was placed into the chamber moutned atop the rotary actuated Stewart platform. The platform was programmed to tilt itself to a specified angle and hold. If the configuration broke within 30s, it was regarded as unstable (Supplementary Figure 2). Typically, triplets would separate into a singlet and doublet. This experiment was repeated for 12 different values of $sin(\alpha)$ between 0.00 and 0.13.

# 3 Basic features of two-component droplets

The basic features associated with the evaporation of two-component Marangoni-contracted droplets have been described previously [4]. It is well known that evaporation at the edge of a droplet is greater than at its center. Thus, when a droplet is composed of two miscible fluids, where one fluid has a higher surface tension and lower vapor pressure (e.g. water and propylene glycol), an effective contact angle $\theta_{eff}$ is observed where otherwise complete wetting is expected. This effective contact angle is due to a Marangoni flow from the droplet apex to its border that seeks to eliminate the vapor-induced surface tension gradient across the droplet. This bulk flow stops the otherwise individual components of the droplet from completely wetting the surface. Across a wide range of concentrations, $\cos(\theta_{eff})$ has been shown to be a linear function of humidity: $cos(\theta_{eff}) = mRH + b$ [4, 5]. Here, $RH$ is non-dimensional and assumes a value between $0 - 100$ and the linear fitting parameters $m$ and $b$ are determined empirically. This humidity dependent contact angle gives rise to the two key features of two-component droplets that are exploited in this work: 1) an absence of pinning and 2) the ability to move under external humidity gradients.

# 4 Behavior of droplet on an inclined plane in one dimension

The behavior of individual two-component droplets subject to an external gravitational force has been studied by the authors previously in a series of inclined plane experiments [5]. Here, we describe the main results of that work. We consider droplets with an average radius $R$, viscosity $\eta$, surface tension $\gamma$, and density $\rho$. Since this problem involves a distribution of droplets with different sizes we let $R \rightarrow aR_i$ to mark the size of the $i^{th}$ droplet. Since $R_i$ is non-dimensional in our notation we must multiply by the characteristic length scale $a$. In one dimension, the scalar velocity $U_i$ of the $i^{th}$ droplet can be estimated by equating the drag

force $F_{drag}$ with the external gravitational force $F_g$. A rough description of $F_{drag}$ is given by:

$$F_{drag} = \frac{\pi a R_i \eta ln(k_1/k_2)}{\theta} U_i \tag{5}$$

In this expression, $U_i$ describes the velocity of the contact line normal to the plane of motion [5]. For convenience, we define $A = \theta/ln(k_1/k_2)$. This term is a numerical factor describing the singular dissipation in the moving droplet [6]. The terms $k_2$ and $k_1$ describe the length scales associated with the details of the physical process of viscous dissipation as the droplet moves. Typically, $k_2$ represents the macroscopic length scale on the order of droplet radius while $k_1$ is more difficult to specify, depending on the dissipation mechanism. For sessile droplets, $k_1$ is on the order of the size of a molecule of water while two-componet droplet have $k_1$ on the order of nanometers [5]. This behavior is similar to droplet motion on liquid infused surfaces [7]. Meanwhile, the force of gravity on a spherical droplet can be described straightforwardly:

$$F_g = \frac{4\pi a^3 R_i^3 \rho g}{3} sin(\alpha) \tag{6}$$

where $g$ is the standard acceleration of gravity and $\alpha$ is the angle of incline. Equating $F_{drag}$ and $F_g$ and solving for $U_i$ gives:

$$U_i = \frac{4a^2 R_i^2 \rho g A}{3\eta} sin(\alpha) \tag{7}$$

In general, a viscous force $F_{drag}$ acting on a particle is proportional to the particle's velocity $U_i$ according to $F_{drag} = C_{drag,i} U_i$, where $C_{drag,i}$ describes viscous damping. As such, we can identify in Equation 7 that $C_{drag,i} = a R_i \eta$. Finally, this expression can be rewritten in terms of a non-dimensional velocity by normalizing with $U_0 = \gamma/\eta$:

$$\frac{U_i}{U_0} = \frac{4a^2 R_i^2 \rho g A}{3\gamma} sin(\alpha) \tag{8}$$

The authors demonstrated that this relationship describes the motion of droplets of varying in size and viscosity. Importantly, and in contrast to sessile droplets, this expression holds true even for small $\alpha$. Typical sessile droplets experience an additive pinning force which restricts their motion below a certain critical angle, two-component droplets experience a negligible pinning force. In other words, the capillary number ($Ca = \frac{\eta}{\gamma}U_i$) is proportional to the Bond number ($Bo = \frac{R^2\rho g}{\gamma}$) according to $Ca \sim Bosin(\alpha)$. The practical consequence of this result is that an inclined plane can be used to make droplets motile. It was noted that above a certain value of $Bosin(\alpha)$, the receding contact line deforms and eventually enter a regime where they emit smaller droplets. Similar behavior has been reported for single-component droplets on inclined planes [8]. We also remark that the effect of gravity on evaporation remains poorly understood [9, 10]. These effects are consequential for the internal Marangoni flow [11, 12] which underlies motility in two-component droplets.

# 5 Force of attraction between neighboring droplets in one dimension

The behavior of pairs of droplets has also been studied previously [4, 13]. A two-component droplet $i$ can move in response to a humidity gradient established by a neighboring droplet $j$ separated by a distance $r_{ij}$. The magnitude of this force is given by $F_a = \gamma a R_i m R H f(R_j, r_{ij})$. Here, $m$ is the slope describing the linear relation between $\theta_{eff}$ and $RH$. The function $f(R_j, r_{ij})$ has previously been identified as the gradient in the vapor concentration established by the $j^{th}$ droplet. Thus, $f(R_j, r_i) = \nabla\phi(R_j, r_{ij})$ and scales with $1/r_{ij}^2$ [3]. Here, the gradient is calculated with respect to the Cartesian coordinates $x$ and $y$. The vapor concentration of a lens-shaped droplet with contact angle $\theta \sim 0^\circ$ can be described by [14]:

$$\phi(R_j, r_{ij}) = \begin{cases} 1 & r_{ij} < R_j \\ \frac{2}{\pi}\arcsin\left(\frac{R_j}{r_{ij}}\right) & r_{ij} \geq R_j \end{cases} \tag{9}$$

The low-contact angle limit is valid based on of experimental values obtained for isolated droplets $\theta \sim 10^{\circ}$ [4]. Further, the contact angle is expected to be further reduced in the high-humidity environment of the droplet array [15]. If we consider a pair of droplets such that the $j^{th}$ droplet is pinned and the $i^{th}$ droplet is free to move, we can obtain the velocity of the mobile droplet from $C_{drag,i}U_i = F_a$. Since $C_{drag,i} = a\eta R_i$:

$$U_i = \frac{2\gamma mRH}{\pi\eta}\nabla \arcsin\left(\frac{R_j}{r_{ij}}\right) \tag{10}$$

As before, this expression can be rewritten in terms of a non-dimensional velocity by normalizing with $U_0 = \gamma/\eta$:

$$\frac{U_i}{U_0} = \frac{2mRH}{\pi}\nabla \arcsin\left(\frac{R_j}{r_{ij}}\right) \tag{11}$$

To extend this expression to account for multi-droplet interactions we introduce a fitting parameter. This approach has been validated in previous work by the present authors [3]. The fitting parameter accounts for non-additive shielding effects without adding significant computational complexity (e.g. explicitly accounting for multi-body interactions). The fitting parameter is denoted by $\xi$ and represents the number of discrete lattice sites before interactions are clipped:

$$\frac{U_i}{U_0} = \frac{2mRH}{\pi}\nabla \sum_{j}^{\mathcal{N}(\xi)} \arcsin\left(\frac{R_j}{r_{ij}}\right) \tag{12}$$

Thus $\mathcal{N}(\xi)$ represent the total number of droplets that are $\xi$ discrete lattice sites away. It was shown that after identifying a suitable value for $\xi$, this description could capture the basic features of relaxation from a high energy to a low energy configuration [3]. The value of $\xi$ was found to be proportional to the density of droplets per area such that dense arrays more efficiently screen their neighbors [3].

# 6 Multi droplets subject to a time-varying field in two dimensions

We have introduced the basic physics describing motion of two-component droplets due to the force of gravity on an inclined plane and the force associated with vapor-mediated attraction between many droplets. We now extend this description to a system of $N$ two-component droplets confined to a hexagonal honeycomb lattice defined in the $x, y$ plane subject to a time-varying external body force.

We begin by defining a vector description for the lattice. The distance $r_{ij}$ between the $i^{th}$ and $j^{th}$ droplets is given by:

$$r_{ij} = \|\vec{\mathrm{P}}_j + \vec{r}_j - \vec{\mathrm{P}}_i - \vec{r}_i\| \tag{13}$$

Where the vectors $\vec{\mathrm{P}}$ describe the position of the unit cell relative to the origin and the vectors $\vec{r_i}$ describe the position of a droplet relative to its unit cell. This is shown schematically in Supplementary Figure 1. In this notation the non-dimensional velocities must be turned into vector quantities: $\frac{U_i}{U_0} \rightarrow \dot{\vec{r_i}}$. Equations 8 and 12 are combined to become:

$$\dot{\vec{r_i}} = \frac{2mRH}{\pi}\vec{\nabla}\sum_{j}^{\mathcal{N}(\xi)} \arcsin\left(\frac{R_j}{r_{ij}}\right) + \frac{4a^2R_i^2\rho g A}{3\gamma} sin(\alpha)\vec{u}(t) \tag{14}$$

where have introduced $\vec{u}(t) = \{sin(\omega t)\hat{x}, cos(\omega t)\hat{x}\}$ to describe the time dependence of the orientation of the external body force.

Finally, we must construct a term to represent the hexagonal potential well to constrain the droplet's motion within the unit cell. The effect of the hydrophobic boundary on the droplet velocity is obtained from $\nabla E_{cell}$. Conceptually, $E_{cell}$ represents the potential well defined by the short ranged repulsive force imposed by the hydrophobic material used to fabricate the lattice pattern. Mathematically, this is represented by a non-dimensional logistic function whose parameters are chosen such that the barrier height is approximately

an order of magnitude greater than the largest possible value of Equation 14:

$$E_{cell} = \frac{-R}{1 + e^{\frac{0.48 - R - z(x,y)}{0.023}}} \tag{15}$$

Here, we have constructed $z(x, y)$ from a function having hexagonal symmetry in the xy-plane. This reflects the unit cells hexagonal symmetry and determines the influence of the boundary given a droplets Cartesian coordinates $(x, y)$:

$$z = \frac{\sqrt{x^2 + y^2}}{\zeta(\kappa)} \tag{16}$$

where $\zeta(\kappa)$ is a Fourier series in multiples of 6 and $\kappa = \arctan \frac{y}{x}$. Explicitly:

$$\zeta(\kappa) = \frac{5389}{5184} - \frac{2}{45}\cos(6\kappa) + \frac{1}{180}\cos(12\kappa) - \frac{2}{2835}\cos(18\kappa) + \frac{1}{20160}\cos(24\kappa) \tag{17}$$

The values of the coefficients $\zeta(\kappa)$ are chosen such that derivatives with respect to $\kappa$ are set equal to zero. This expression yields a boundary profile with hexagonal symmetry. The potential produced by this function is shown in Supplementary Fig. 1.

We now add this final term to Equation 14 to obtain the equation of motion for the multi-droplet system subject to a time-varying external body force:

$$\dot{\vec{r}} = \frac{2mRH}{\pi}\vec{\nabla}\sum_{j}^{\mathcal{N}(\xi)} \arcsin\left(\frac{R_j}{r_{ij}}\right) + \frac{4a^2R_i^2\rho g A}{3\gamma} sin(\alpha)\vec{u}(t) + \vec{\nabla}E(\vec{r}) \tag{18}$$

The sharp boundary that the term $\vec{\nabla}E(\vec{r})$ creates makes this a system of stiff differential equations and so they are integrated using a suitable method such as the backwards difference formula as implemented by the NDSolve function in Mathematica.

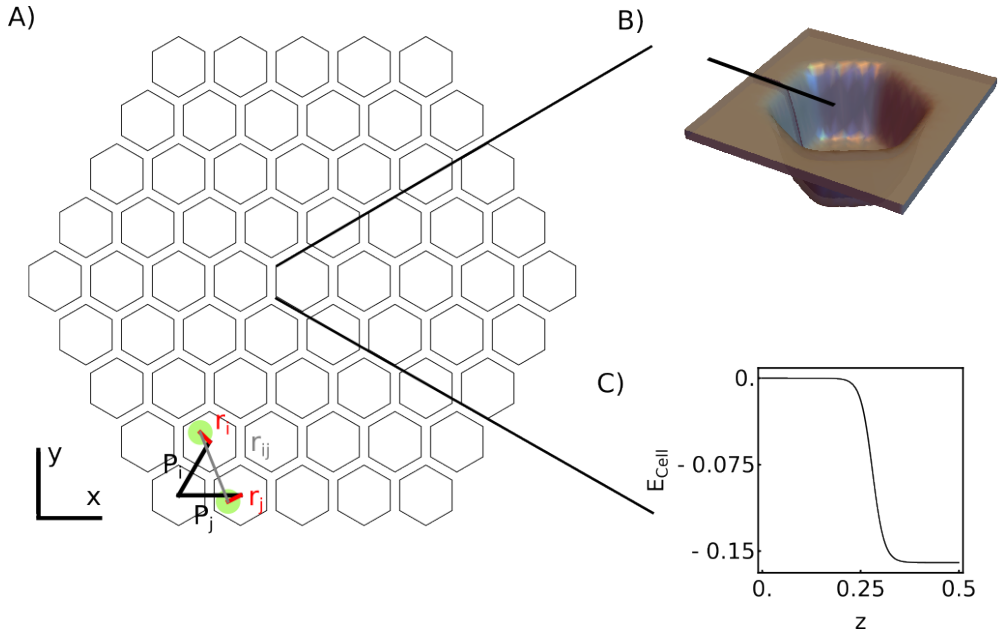


**Supplementary Figure 1:** ( A) schematic showing the geometry of the hexagonal honeycomb lattice. The vectors $\vec{P}$ represent the distance from the origin to the center of a given unit cell and the vectors $\vec{r}$ represent the distance from the center of the unit cell a droplet's instantaneous position. The origin is located at the center of the unit cell in the bottom left. (B) Three dimensional plot of the cell boundary defined by $E_{cell}$. (C) A cross section is obtained by plotting $E_{cell}$ against $z$ as described in Equation 15, highlighting the steepness of the boundary.

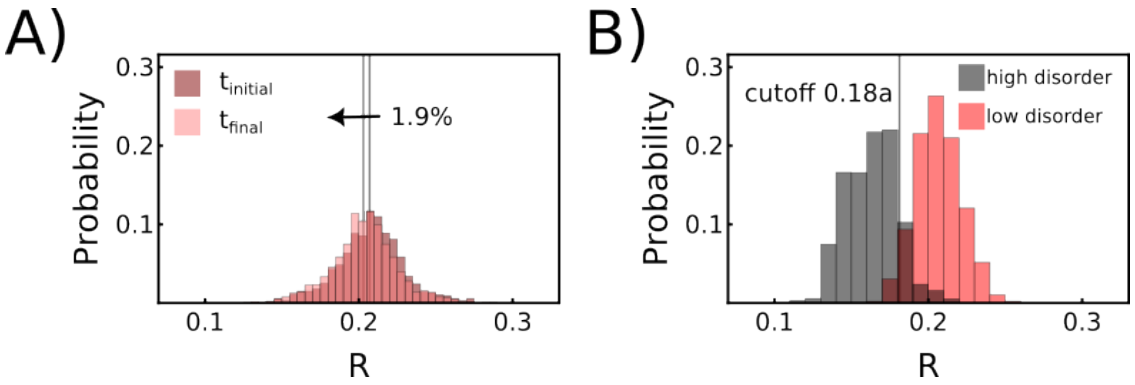


**Supplementary Figure 2:** Size distribution of droplets. (A) distribution of droplets used to obtain experimental phase diagram in Fig. 2. Measurement of non-dimensional droplet radius at $t_{initial} = 0\ s$ when rotation starts and $t_{final}$ when rotation stops, show an average 1.9% reduction in size. (B) distribution for the two systems represented in Fig. 4. The high disorder distribution is centered at $R = 0.21a$ with $n = 10.1\%$ and the low disorder distribution is centered at $R = 0.18a$ with $n = 8.9\%$. The vertical line indicates a threshold below which droplets show limited mobility when the system is driven with field amplitude $\sin(\alpha) = 0.095$.

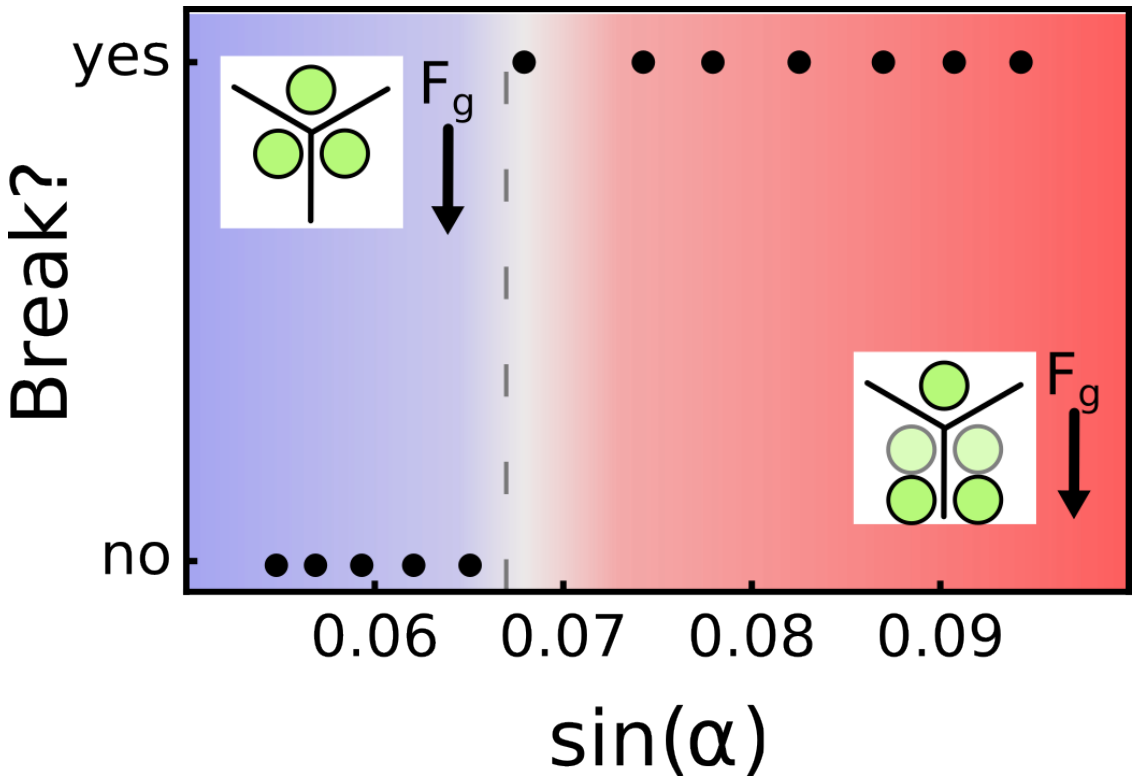


**Supplementary Figure 3:** Experimental data for a set of inclined plane experiments subjecting an individual triplet configuration to an increasing body force. Each data point represents an independent experiment. A configuration is considered unbroken if it remains stable after 30s. Insets are cartoon illustrations corresponding to a broken and unbroken triplet. The arrow indicates the direction of gravity.

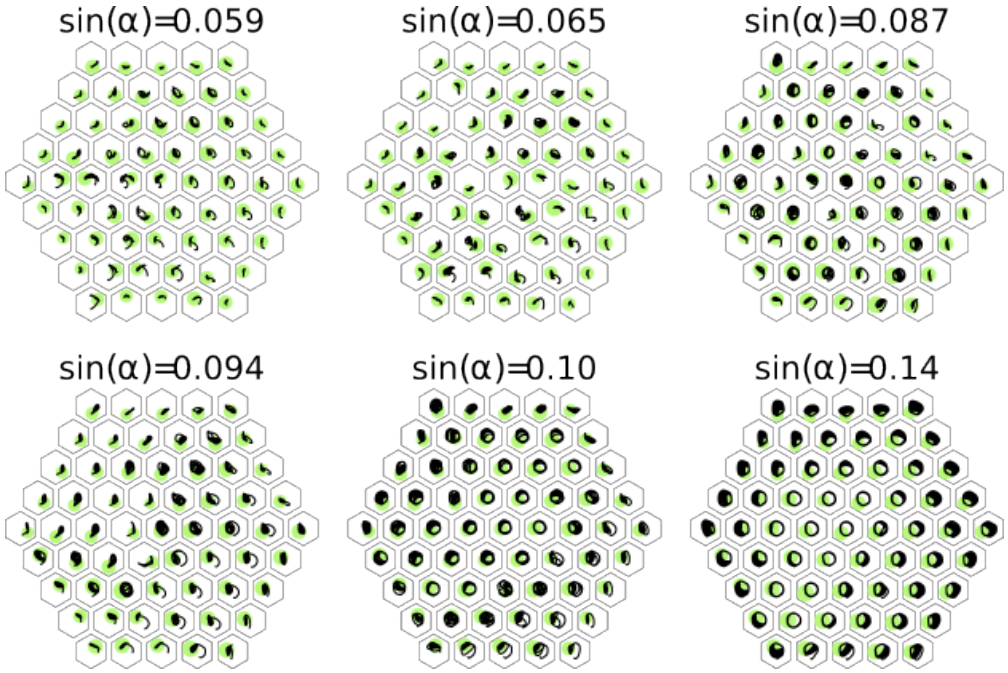


**Supplementary Figure 4:** Trajectories of individual droplets shown for a selection of values for $sin(\alpha)$ obtained from experimental realizations at $\omega t_0 = 1.61(< R >= 0.18a$, noise=10.1%). Fig. 3A is obtained from this data.

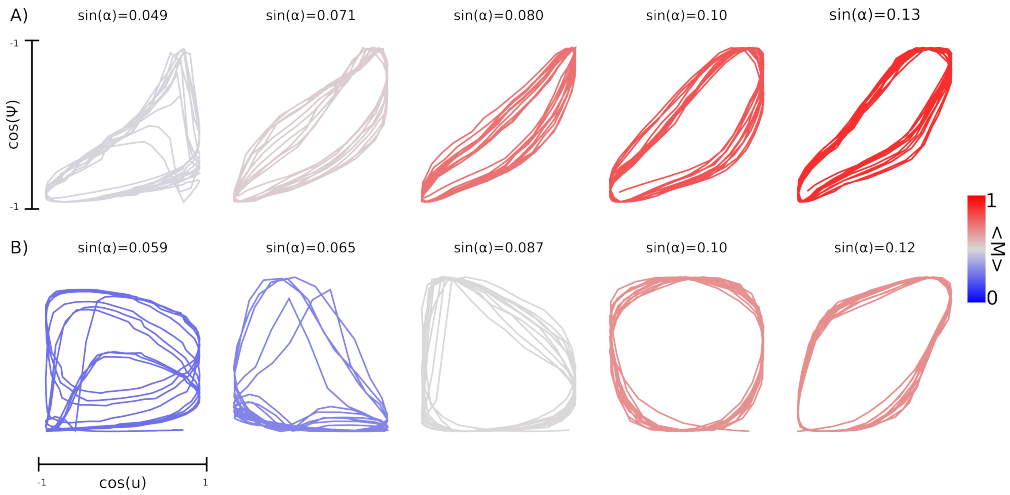


**Supplementary Figure 5:** Hysteresis loops measured as a function of $sin(\alpha)$ for systems with droplet radius (A) $< R >= 0.21a$, noise= 10.1% ($\omega t_0 = 1.34$) and (B) $< R >= 0.18a$, noise= 8.9% ($\omega t_0 = 2.04$). For each loop the horizontal axis is the orientation of the applied field and the vertical axis is magnetization. The loops are colored according to their average magnetization according to the color scheme described in Fig. 2

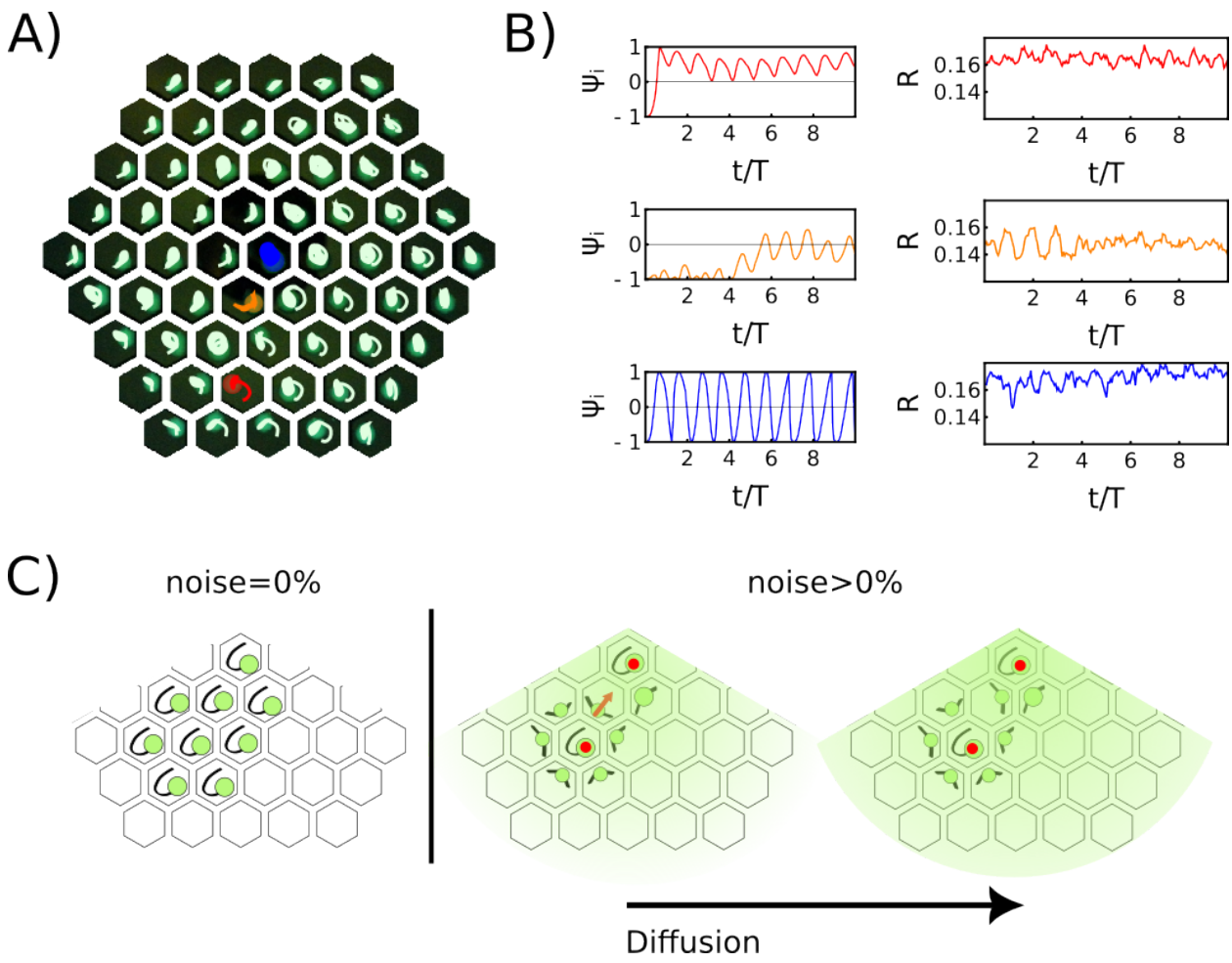


**Supplementary Figure 6:** Microscopic dynamics in transition region depends on droplet size and local environment. (A) Droplet trajectories for an experiment conducted at $\sin(\alpha) = 0.095$ and $\omega t_0 = 2.04$ (Fig. 4E) with three droplets highlighted. (B) Time evolution of $\psi$ (left) and radius $R$ (right) for the highlighted droplets in (A) corresponding to fixed (red), migrating (orange), and field-driven (blue) droplets. (C) Cartoon illustration showing possible scenarios where diffusion and details of neighboring droplets work together to create migratory droplet behavior. Droplets marked with red are large enough such that they are fully mobilized by the applied field - as a result their motion is governed by the applied field. The motion of smaller droplets (unmarked) is influenced by their proximity to larger droplets. As vapor accumulates in the center of the system, the likelihood of a droplet migrating towards the center of the system increases leading to other rearragenments within the system. Migrating droplets are an example of non-trivial dynamics.

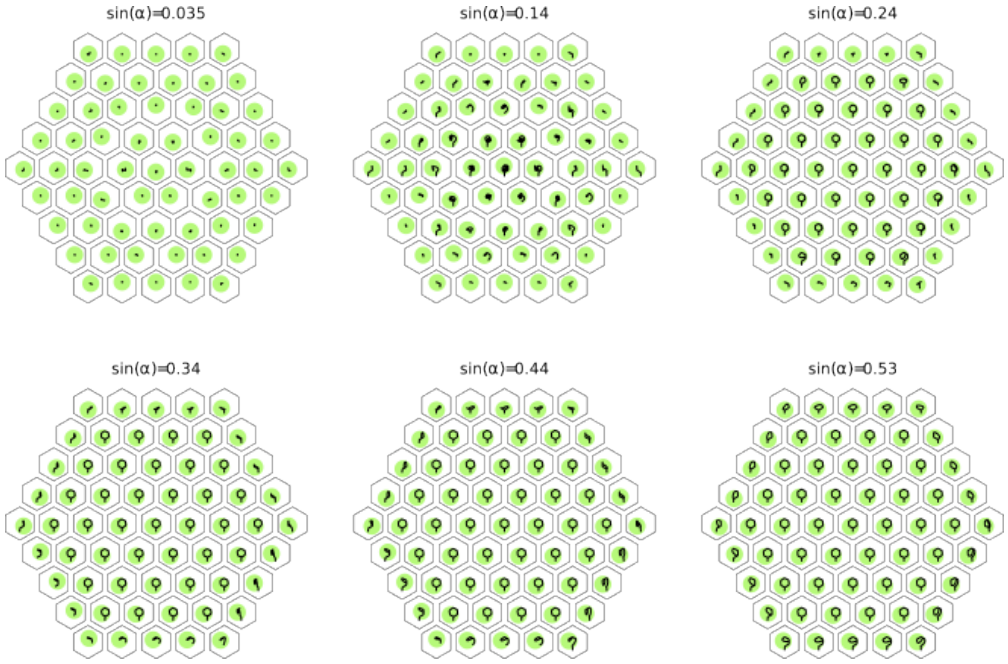


**Supplementary Figure 7:** Trajectories of individual droplets shown for a selection of values for $sin(\alpha)$ obtained from numerical simulation at $\omega t_0 = 0.78$ ($R = 0.25a$, noise=0%).

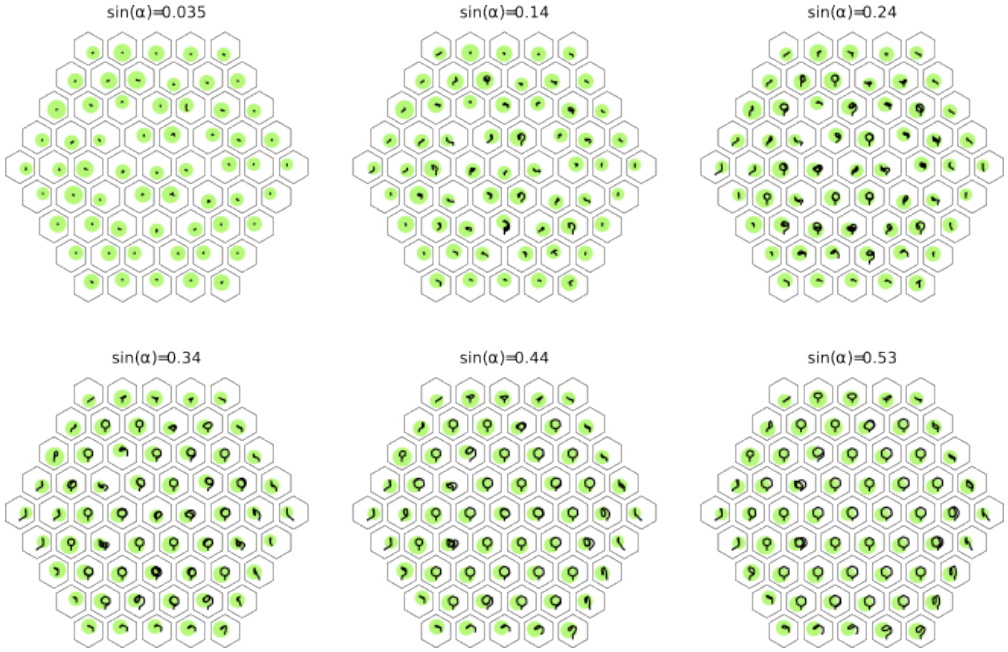


**Supplementary Figure 8:** Trajectories of individual droplets shown for a selection of values for $sin(\alpha)$ obtained from numerical simulation $\omega t_0 = 0.78$ ($R = 0.225a$, noise=10%).

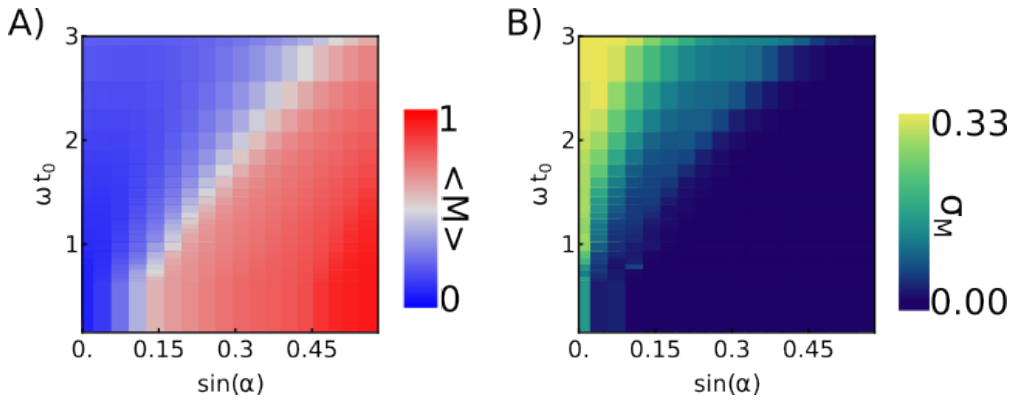


**Supplementary Figure 9:** Effect of different sources of noise on numerical phase diagram. Numerical phase diagram (A) and variance (B) for uniform droplets ($R = 0.25a$) with 5% noise in initial position. Simulations were fixed with $\xi = 2$ and each diagram represents $N = 6$ different random initial conditions.

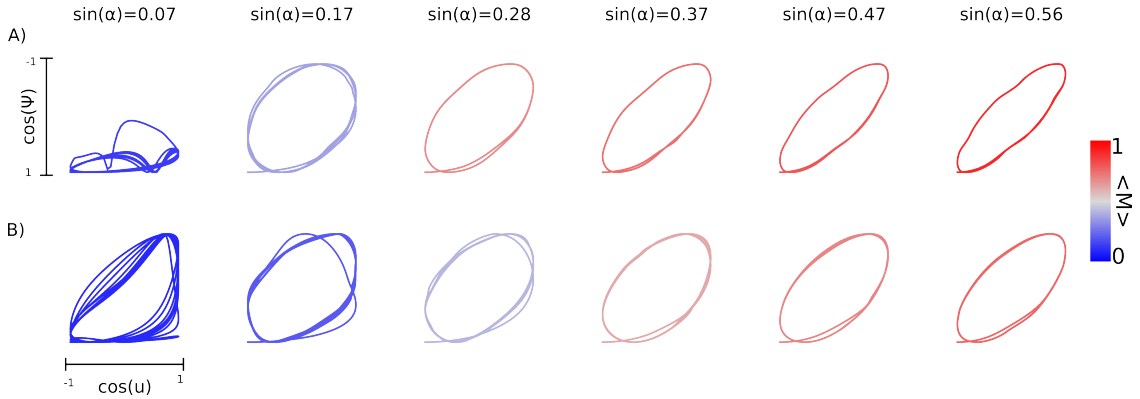


**Supplementary Figure 10:** Hysteresis loops obtained from simulation data at ($\omega t_0 = 0.78$) with (A) uniform droplet size ($R = 0.25a$, noise= 0) and (B) disordered droplet size ($R = 0.225a$, noise= 10%). For each loop the horizontal axis is the orientation of the applied field and the vertical axis is magnetization. The loops are colored according to their average magnetization according to the color scheme described in Fig. 2.

**Supplementary Video 1:** Experimental set showing preparation of a droplet tiling, placement in an enclosed chamber, and implementation of rotating gravitational field using a Stewart platform.

**Supplementary Video 2:** Transition from interaction- to field-dominated behavior controlled by strength of rotating gravitational field. Representative data for three distinct phases are shown. The orientation of droplets are annotated according the scheme in Fig. 2.

**Supplementary Video 3:** Strongly, driven large droplets leave behind a trail of their own constituents.

**Supplementary Video 4:** Mesoscale structures emerge at the onset of transition region. The qualitative features of the structures depend on the spatial distribution of field-couplings. The orientation of droplets are annotated according to the scheme in Fig. 2. Bond Lengths between neighboring droplets are annotated according to the scheme in Fig. 4.

**Supplementary Video 5:** Annealing of the frustrated centered hexagonal honeycomb lattice ($N = 61$). The orientation of droplets are annotated according to the scheme in Fig. 2. Bond Lengths between neighboring droplets are annotated according to the scheme in Fig. 4.

**Supplementary Video 6:** Numerical simulation showing the transition from interaction-dominated to field-dominated behavior at $\omega/\omega_0 = 160$ for a system with $R = 0.225a$ and noise=10%. The interaction lengthscale is set to $\xi = 2$

# References


[1] Stewart, D. A platform with six degrees of freedom. *Proceedings of the Institution of Mechanical Engineers* **180**, 371–386 (1965).

[2] Patel, V., Krishnan, S., Goncalves, A. & Goldberg, K. Sprk: A low-cost stewart platform for motion study in surgical robotics. *2018 International Symposium on Medical Robotics (ISMR)* (2018).

[3] Molina, A., Kumar, S., Karpitschka, S. & Prakash, M. Droplet tilings for rapid exploration of spatially constrained many-body systems. *Proceedings of the National Academy of Sciences* **118**, e2020014118 (2021).

[4] Cira, N., Benusiglio, A. & Prakash, M. Vapour-mediated sensing and motility in two-component droplets. *Nature* **519**, 446–450 (2015).

[5] Benusiglio, A., Cira, N. J. & Prakash, M. Two-component marangoni-contracted droplets: friction and shape. *Soft Matter* **14**, 7724–7730 (2018).

[6] de Gennes, P. G. Wetting: statics and dynamics. *Reviews of Modern Physics* **57**, 827–863 (1985).

[7] Keiser, A., Keiser, L., Clanet, C. & Quéré, D. Drop friction on liquid-infused materials. *Soft Matter* **13**, 6981–6987 (2017).

[8] Le Grand, N., Daerr, A. & Limat, L. Shape and motion of drops sliding down an inclined plane. *Journal of Fluid Mechanics* **541**, 293–315 (2005).

[9] Kim, J. Y., Hwang, I. G. & Weon, B. M. Evaporation of inclined water droplets. *Scientific Reports* **7**, 42848 (2017).

[10] Timm, M. L., Dehdashti, E., Jarrahi Darban, A. & Masoud, H. Evaporation of a sessile droplet on a slope. *Scientific Reports* **9**, 19803 (2019).

[11] Du, X. & Deegan, R. D. Ring formation on an inclined surface. *Journal of Fluid Mechanics* **775**, R3 (2015).

[12] Sáenz, P. J. *et al.* Dynamics and universal scaling law in geometrically-controlled sessile drop evaporation. *Nature Communications* **8**, 14783 (2017).

[13] Benusiglio, A., Cira, N., Lai, A. W. & Prakash, M. Two-component self-contracted droplets: long-range attraction and confinement effects. *arXiv:1711.06404* (2017).

[14] Eggers, J. & Pismen, L. M. Nonlocal description of evaporating drops. *Physics of Fluids* **22**, 112101 (2010).

[15] Carrier, O. *et al.* Evaporation of water: evaporation rate and collective effects. *Journal of Fluid Mechanics* **798**, 774–786 (2016).